Journal of Fluids and Structures 85 (2019) 138–148

Contents lists available at ScienceDirect

Journal of Fluids and Structures

journal homepage: www.elsevier.com/locate/jfs

Forced vibrations as a mechanism to suppress flutter—An aeroelastic Kapitza's pendulum

Ofek Peretz, Amir D. Gat *

Faculty of Mechanical Engineering, Technion - Israel Institute of Technology, Haifa, Israel

ARTICLE INFO

Article history:
Received 23 January 2018
Received in revised form 8 November 2018
Accepted 21 December 2018
Available online xxxx

Keywords:
Aeroelasticity
Flutter
Kapitza's pendulum
Parametric excitation

ABSTRACT

Inspired by Kapitza's inverted pendulum, forced vibrations are suggested as a mechanism to suppress aeroelastic flutter. We examine high-frequency small-amplitude vibrations (e.g. by an internal oscillating mass) applied on a 2D airfoil, yielding forced periodic excitation in the gyration-radius. Under such excitation, the aeroelastic dynamics involve time-periodic system of two Hill-type ODEs. Harmonic balance is applied, along with Floquet theory approach, in order to find approximated transition curves between stable and unstable regions. The transition curves are obtained from the relevant Hill's determinants, and are validated by numerical calculations. Structural 3D effects are examined by the aeroelastic strip approach for excitation in a section or the entire wing. The results indicate that rapid small-amplitude oscillations can significantly increase the maximal stable velocity in realistic flight conditions.

1. Introduction

This work analyzes the aeroelastic dynamics of a two-dimensional wing section under the effect of forced parametric excitation. Specifically, rapid small-amplitude vibrations of the airfoil's gyration-radius are examined as a mechanism to modify the transition curves between stable and unstable regions, and thus suppress flutter instability. Flutter is a potentially destructive phenomenon which occurs in flexible structures subjected to aerodynamic forces, such as aircraft (Garrick and Reed III, 1981; Yang and Zhao, 1988), buildings (Kawai, 1998; Hübner et al., 2004) and bridges (Borri et al., 2002; Ostenfeld-Rosenthal et al., 1992; Scanlan, 1978). Flutter occurs due to the interaction between the aerodynamic forces, structure stiffness and inertial forces. As the flow speed increases, solid deformation and inertia due to aerodynamic forces increase as well, and at a certain velocity, the structure will lose stability, which may result in structural failure. Loss-of-stability commonly occurs due to deformation which diverges monotonically (known as divergence Weisshaar, 1980) or structural oscillations with an increasing amplitude (known as flutter).

A significant part of modern aircraft design is focused on avoiding the onset of flutter instability. Current methods to limit or eliminate flutter include: (a) Uncoupling the torsion and bending moment by changing the wing mass distribution or stiffness (Hollowell and Dugundji, 1984; Kameyama and Fukunaga, 2007). (b) Energy dissipation by the use of a tuned-mass–damper (Li, 2000; Gu et al., 1998; Kwon and Park, 2004), composed of a mass, spring and a viscous damper tuned to a specific natural frequency. (c) Another technique applies active control on aerodynamic surfaces as active-flutter-suppression (Karpel, 1982; Livne, 2017; Friedmann et al., 1997; Lhachemi et al., 2017; Reich et al., 2004; Xiang et al., 2014;

* Corresponding author.
E-mail addresses: ofekperetz@campus.technion.ac.il (O. Peretz), amirgat@technion.ac.il (A.D. Gat).
URL: http://gat.net.technion.ac.il (A.D. Gat).

https://doi.org/10.1016/j.jfluidstructs.2018.12.008
0889-9746/

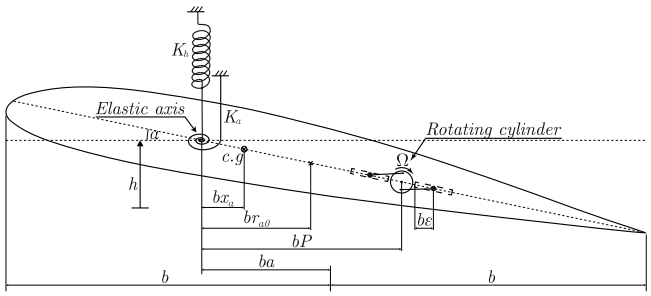

Fig. 1. Illustration of the examined configuration. A rigid airfoil is connected to vertical displacement and torsion springs, and include a mechanism which rapidly oscillates two small internal masses in frequency Ω over distance $b\varepsilon$. In the presented configuration the masses move in opposite directions so that the center-of-mass remains constant.

Li et al., 2012). This technique uses measurements taken on the vehicle in order to generate motion on the control surfaces which applies aerodynamic forces in such a way that the overall forces suppress flutter.

The current work is inspired by previous studies on stabilization of an inverted pendulum by application of high-frequency vertical vibrations on the pendulum's pivot (Kapitza, 1951). This phenomenon, named after Pyotr Kapitza who was the first to explain it successfully, is governed by a differential equation which contains parametric excitation (Hsu, 1963). The set of differential equations governing aeroelastic dynamics under periodic excitation of gyration-radius similarly involve parametric excitation and resemble Hill's and Mathieu's equations (Magnus and Winkler, 2013). Thus, Floquet theory (Kuchment, 2012) and harmonic balance (Mickens, 2010) are applied in order to analytically determine the effect of high-frequency low-amplitude excitation on the transition curves between stable and unstable regions.

The structure of this work is as follows. In Section 2 problem definition and derivation of governing equations are introduced. In Section 3 harmonic balance is applied to obtain transition curves between stable and unstable regions. In Section 4 governing equations are solved numerically in order to validate the analytic results and determine the stability regions. In Section 5 a simplified quasi-3D configuration is examined. In Section 6 concluding remarks are provided.

2. Problem definition and governing equations

The aeroelastic model used is a two-dimensional spring-supported rigid wing segment (Bisplinghoff et al., 1957), containing a reactionless oscillating mass (m_a). The mass m_a may oscillate via connection to a cylinder rotating at constant frequency, or by other methods, yielding a periodic change in the gyration-radius and the center-of-mass of the airfoil. The examined configuration is illustrated in Fig. 1. The degrees-of-freedom of the examined airfoil are angular rotation α and vertical displacement $\tilde{h}$. The chord length is $2b$ and other geometric parameters are measured from the center of the chord. The distance between the chord middle to the elastic axis is ba. The distance between the elastic axis and the center-of-mass, multiplied by the total mass, is $S_\alpha = (m + m_a)bx_\alpha$. The torsion spring stiffness is K_α and vertical displacement spring stiffness is K_h. In addition, an internal mass oscillates at a forced frequency Ω and amplitude of $b\varepsilon$. The distance between the chord middle and the mechanism center-of-mass is P. The flight speed is V. The wing moment of inertia around the elastic axis is I_α, the wing segment's mass is m (excluding the oscillating mass m_a) and ρ is air density. In addition, we define reduced oscillation's frequency $k = \omega b/V$, dimensionless gyration radius $r_\alpha = (I_\alpha/(m + m_a)\, b^2)^{1/2}$, density ratio $\mu = (m + m_a)/\pi\rho b^2$, uncoupled natural bending frequency $\omega_h = (K_h/(m + m_a))^{1/2}$ and uncoupled natural torsion frequency $\omega_\alpha = (K_\alpha/I_\alpha)^{1/2}$. Scaled heave is $h = \tilde{h}/b$. With the exception of frequencies, all parameters are defined per-unit-length.

The kinetic T and potential U energies of the configuration are given by

$$T = \frac{1}{2}(m + m_a)\dot{\tilde{h}}^2 + \frac{1}{2}I_\alpha\dot{\alpha}^2 + S_\alpha\dot{\tilde{h}}\dot{\alpha}, \tag{1a}$$

$$U = \frac{1}{2}K_h\tilde{h}^2 + \frac{1}{2}K_\alpha\alpha^2 \tag{1b}$$

and substituting (1) into the Lagrange's equations (see chapter 3 in Fabien, 2008) yields the relevant system of equations of motion

$$(m + m_a)\ddot{\tilde{h}} + S_\alpha\ddot{\alpha} + \dot{S}_\alpha\dot{\alpha} + K_h\tilde{h} = -L, \tag{2a}$$

$$S_\alpha\ddot{\tilde{h}} + I_\alpha\ddot{\alpha} + \dot{S}_\alpha\dot{\tilde{h}} + \dot{I}_\alpha\dot{\alpha} + K_\alpha\alpha = M_y, \tag{2b}$$

where L and M_y are aerodynamic lift and moment around the elastic axis. The governing equations (2) differ from the standard model (Bisplinghoff et al., 1957) by the terms $\dot{S}_\alpha\dot{\alpha}$ and $\dot{I}_\alpha\dot{\alpha}$, since both I_α and S_α are time-dependent due to the forced oscillations. Substituting x_α, r_α, h, ω_h and ω_α, and applying standard Theodorsen's theorem (Caracoglia and Jones, 2003) $L = L_h h + L_{\dot{h}}\dot{h} + L_\alpha\alpha + L_{\dot{\alpha}}\dot{\alpha}$ and $M_y = M_h h + M_{\dot{h}}\dot{h} + M_\alpha\alpha + M_{\dot{\alpha}}\dot{\alpha}$ for an unsteady aerodynamic model (described in Appendix A) and under the assumptions of incompressible flow and small deformations, Eqs. (2) can be presented in the form

$$\begin{bmatrix} 1 & x_\alpha \\ x_\alpha & r_\alpha^2 \end{bmatrix} \begin{Bmatrix} \ddot{h} \\ \ddot{\alpha} \end{Bmatrix} + \left(\begin{bmatrix} 0 & \dot{x}_\alpha \\ \dot{x}_\alpha & 2\dot{r}_\alpha r_\alpha \end{bmatrix} + \frac{bV}{\pi\mu} \begin{bmatrix} L_{\dot{h}} & L_{\dot{\alpha}} \\ -M_{\dot{h}} & -M_{\dot{\alpha}} \end{bmatrix} \right) \begin{Bmatrix} \dot{h} \\ \dot{\alpha} \end{Bmatrix} + \left(\begin{bmatrix} \omega_h^2 & 0 \\ 0 & r_\alpha^2\omega_\alpha^2 \end{bmatrix} + \frac{V^2}{\pi\mu} \begin{bmatrix} L_h & L_\alpha \\ -M_h & -M_\alpha \end{bmatrix} \right) \begin{Bmatrix} h \\ \alpha \end{Bmatrix} = \begin{Bmatrix} 0 \\ 0 \end{Bmatrix}. \tag{3}$$

While an oscillating mass can generate a change in both center-of-mass and gyration-radius, for simplicity only a specific case where two equal masses oscillate contrary around the mechanism's center is examined hereafter. This results in a constant center-of-mass and an oscillating gyration-radius, therefore r_α is time dependent and $\dot{x_\alpha} = 0$.

3. Harmonic balance analysis

Transition curves separate unstable regions from stable regions and involve bounded periodic solutions. According to Floquet theory, Hill-type equations allow periodic solutions with the period T or $2T$ only if the associated parameters values lie on a transition curve (Zounes and Rand, 1998). Harmonic balance is a technique for generating approximated analytic expressions for the transition curves. Under this method, we define the bounded solution $q(t)$, known to be periodic, by the following Fourier series

$$\boldsymbol{q}(t) = \begin{Bmatrix} h \\ \alpha \end{Bmatrix} = \sum_{n=0}^{\infty} \left[\begin{Bmatrix} a_n \\ b_n \end{Bmatrix} \cos\left(\frac{n\Omega t}{2}\right) + \begin{Bmatrix} c_n \\ d_n \end{Bmatrix} \sin\left(\frac{n\Omega t}{2}\right) \right]. \tag{4}$$

The periodic coefficients, obtained by substituting the excitation in the radius of gyration, are denoted by $r_\alpha^2(t) = r_{\alpha 0}^2 m/(m+m_a) + \left(P^2 + \varepsilon^2\cos^2(\Omega t)\right) m_a/(m+m_a)$. Substituting $r_\alpha^2(t)$ into (3) yields

$$\begin{bmatrix} 1 & x_\alpha \\ x_\alpha & r^2_{\alpha 0 m/(m+m_a) + \left(P^2+\varepsilon^2\cos^2(\Omega t)\right) m_a/(m+m_a)} \end{bmatrix} \ddot{q} + \left(\begin{bmatrix} 0 & 0 \\ 0 & -2\Omega\varepsilon^2\cos(\Omega t)\sin(\Omega t)\, m_a/(m+m_a) \end{bmatrix} + \frac{bV}{\pi\mu} \begin{bmatrix} L_{\dot{h}} & L_{\dot{\alpha}} \\ -M_{\dot{h}} & -M_{\dot{\alpha}} \end{bmatrix} \right) \dot{q} + \left(\begin{bmatrix} \omega_h^2 & 0 \\ 0 & \omega_\alpha^2(r_{\alpha 0}^2 m/(m+m_a) + \left(P^2+\varepsilon^2\cos^2(\Omega t)\right) m_a/(m+m_a)) \end{bmatrix} + \frac{V^2}{\pi\mu} \begin{bmatrix} L_h & L_\alpha \\ -M_h & -M_\alpha \end{bmatrix} \right) q = \begin{Bmatrix} 0 \\ 0 \end{Bmatrix}. \tag{5}$$

We continue to substitute (4) into (5) and utilize trigonometric relations to eliminate terms of forms such as $\sin(\Omega t)\sin(n\Omega t/2)$ and $\sin(\Omega t)\cos(n\Omega t/2)$ in order to present (5) solely in terms of the orthogonal functions $\sin(n\Omega t/2)$ and $\cos(n\Omega t/2)$. Thus, Eqs. (5) take the form of

$$\sum_{n=0}^{\infty} \left\{ \begin{bmatrix} -\left(\frac{nVL_{\dot{h}}}{b\pi\mu}\right) a_n - \left(\frac{nVL_{\dot{\alpha}}}{\pi\mu}\right) b_n + \\ \left(w_h^2 - n^2 + \frac{V^2 L_h}{b^2\pi\mu}\right) c_n + \left(-x_\alpha n^2 + \frac{V^2 L_\alpha}{b\pi\mu}\right) d_n \end{bmatrix} \sin\left(\frac{n\Omega t}{2}\right) + \begin{bmatrix} \left(w_h^2 - n^2 + \frac{V^2 L_h}{b^2\pi\mu}\right) a_n + \left(-x_\alpha n^2 + \frac{V^2 L_\alpha}{b\pi\mu}\right) b_n + \\ \left(\frac{nVL_{\dot{h}}}{b\pi\mu}\right) c_n + \left(\frac{nVL_{\dot{\alpha}}}{\pi\mu}\right) d_n \end{bmatrix} \cos\left(\frac{n\Omega t}{2}\right) \right\} = 0. \tag{6a}$$

and

$$\sum_{n=0}^{\infty}\left\{\begin{bmatrix}\left(\frac{nVM_{\dot{h}}}{\pi\mu}\right)a_n+\left(\frac{bnVM_{\dot{\alpha}}}{\pi\mu}\right)b_n+\left(-x_\alpha n^2+\frac{V^2M_h}{b\pi\mu}\right)c_n\\ +\frac{m_a\varepsilon^2\left(\omega_\alpha^2-(n-1)(n-1+\Omega)\right)}{b^2(m+m_a)}d_{n-1}\\ +\left(\frac{\left(2m_aP^2+b^2(m+m_a)r_\alpha^2\right)\left(n^2-w_\alpha^2\right)}{b^2(m+m_a)}-\frac{V^2M_\alpha}{\pi\mu}\right)d_n\\ +\left(\frac{m_a\varepsilon^2\left((n-1)(n-1+\Omega)-\omega_h^2\right)}{b^2(m+m_a)}\right)d_{n+1}\end{bmatrix}\sin\left(\frac{n\Omega t}{2}\right)\right.$$

$$\left.+\begin{bmatrix}\left(-x_\alpha n^2+\frac{V^2M_h}{b\pi\mu}\right)a_n+\frac{m_a\varepsilon^2\left(\omega_\alpha^2-(n-1)(n-1+\Omega)\right)}{b^2(m+m_a)}b_{n-1}\\ +\left(\frac{\left(2m_aP^2+b^2(m+m_a)r_\alpha^2\right)\left(n^2-w_\alpha^2\right)}{b^2(m+m_a)}-\frac{V^2M_\alpha}{\pi\mu}\right)b_n\\ +\left(\frac{m_a\varepsilon^2\left((n-1)(n-1+\Omega)+\omega_h^2\right)}{b^2(m+m_a)}\right)b_{n+1}\\ +\left(\frac{nVM_{\dot{h}}}{\pi\mu}\right)c_n+\left(\frac{bnVM_{\dot{\alpha}}}{\pi\mu}\right)d_n\end{bmatrix}\cos\left(\frac{n\Omega t}{2}\right)\right\}=0. \tag{6b}$$

Since all time-dependent terms are of the form of the orthogonal functions $\sin(n\Omega t/2)$ and $\cos(n\Omega t/2)$, satisfying equations (6a) and (6b) requires the sums of each set of terms multiplying $\sin(n\Omega t/2)$ or $\cos(n\Omega t/2)$ to separately equal zero for each value of n. Thus, an infinite set of linear homogeneous equations for $\{a_n, b_n, c_n, d_n\}$ is obtained and could be represented as a coefficients matrix. In order for $q(t)$ to be a nontrivial solution of the system, the determinant of the coefficient matrix, known as Hill's infinite determinant (Magnus, 1955), must vanish. Equating the determinant to zero establishes a functional relation between Ω and ε, which plots as a transition curve in the $\Omega-\varepsilon$ plane and represents the stability threshold.

The analytic approximation presented in Fig. 2 was generated using symbolic calculations by MATHEMATICA® software for a truncated Fourier series consisting of $N=12$ terms (code is attached as supplementary material). For the presented solution of (6a) and (6b), characteristic values of aircraft parameters were chosen as

$$\mu=100,\quad a=0.25,\quad \omega_h=0.8,\quad \omega_\alpha=1,\quad C_{L_\alpha}=2\pi,\quad b=1[m], \tag{7a}$$

$$m_a=0.1m,\quad P=0.3,\quad x_\alpha=0,\quad r_{\alpha 0}=0.77. \tag{7b}$$

Based on the standard $V-g$ method (Bisplinghoff et al., 1957), the flutter speed V_F and the relevant reduced oscillation frequency k for configurations without excitation ($\Omega=0$, $\varepsilon=0$) are calculated as

$$V_F=3.18[m/s],\quad k=0.279. \tag{7c}$$

(Numerical calculations, presented in Section 4, yielded that the reduced oscillation frequency k is identical for both the unexcited and excited configurations.)

Stability maps obtained by harmonic balance are presented in Fig. 2 for different flight conditions and parameters. The harmonic balance analysis generates the transition curves separating between stable and unstable regions. Since the stability or instability of each region is unknown, a point (set of Ω and ε) in each region is numerically checked. An example to this process is given in Fig. 3. For all panels $V=1.1V_F$ is selected in order to examine the effect of forced actuation on an initially unstable configuration. In each panel a single parameter changes while the rest are kept at the default values prescribed in (7a). All panels show a mostly inverse proportion between ε and Ω required to obtain flutter suppression. Panel (a) presents the case where all parameters are kept as default and the oscillating mass is varied to $m_a\in[0.05, 0.1, 0.15]\cdot m$. The results show that the efficiency of the actuation mechanism increases monotonically with the oscillating mass m_a. Panel (b) presents the case where $x_\alpha=0.1$ and the distance between the elastic axis and the chord middle is set to be $a\in[0.15, 0.25, 0.35]$. A single transition curve separating unstable region (1, U) and stable region (2, S) is obtained for all cases except for $a=0.35$. In this case, we get an additional transition curve defining the stable region (3, S) located within (2, S) and therefore only represents inflection. Panel (c) presents the case where all parameters are kept as default and the flight velocity is varied to $V\in[1.1, 1.2, 1.3]\cdot V_F$. In this case, the reduced oscillation's frequency was calculated separately for each value of V. The results show that the change in the flight velocity only slightly affects the $\Omega-\varepsilon$ transition curve. Panel (d) presents the case where $x_\alpha\in[-0.2, 0, 0.2]$. The transition curve is similar to that of panel (b), where the additional transition curve marks a small stable region (3, S) within unstable (1, U). In the next section, this stability map is validated by numerical solution of the governing equations of motion.

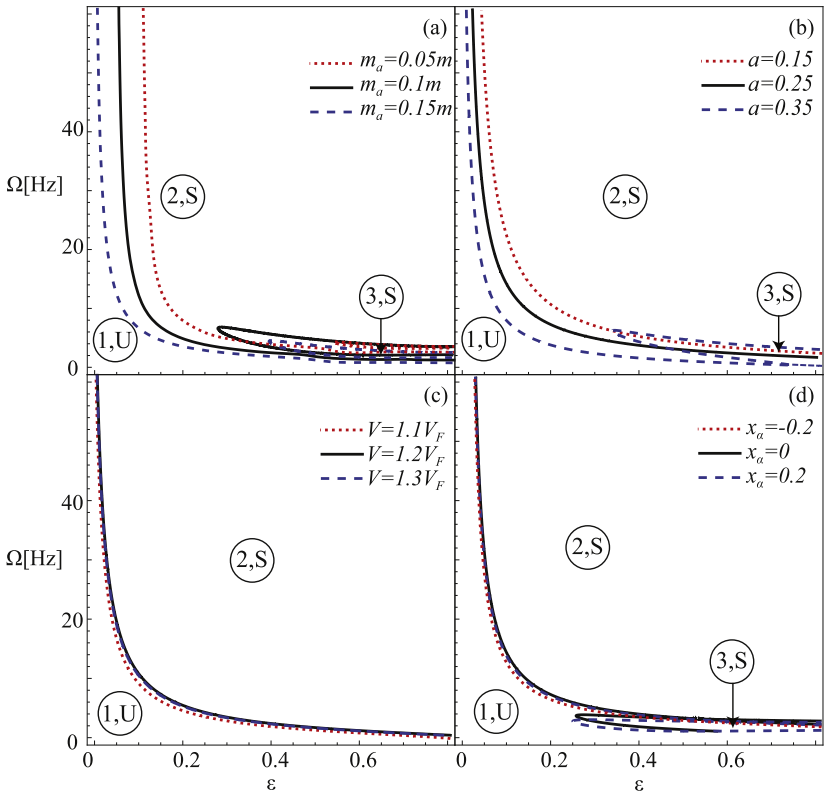

Fig. 2. Approximated transition curves calculated by harmonic balance (6). Stable regions are marked by S and unstable regions are marked by U. In each panel all parameters were kept constant according with values defined by (7) at flight speed $V = 1.1V_F$, except for the variation of a single parameter: (a)-$m_a \in [0.05, 0.1, 0.15]$, (b)-$a \in [0.15, 0.25, 0.35]$, (c)-$V \in [1.1, 1.2, 1.3] \cdot V_F$ and (d)-$x_\alpha \in [-0.2, 0, 0.2]$.

4. Numerical validation

Eqs. (5) were solved numerically using a standard commercially available code (MATLAB® numerical solver ODE45) for various values of excitation parameters. Based on these calculations, an illustrative example of an airfoil in unstable conditions, and stabilization by rapid forced oscillations, is presented in Fig. 3. The parameters used in the computations are defined in (7a). Flutter speed of the unexcited configuration was calculated by a standard $V-g$ method and is presented in (7c). Flight speed is $V = 1.1V_f$. Thus, flutter instability is expected in the absence of stabilizing mechanisms, as indeed evident in panel (a) presenting diverging heave h (blue dashed) and angle-of-attack α (red smooth). Panel (b) presents heave h and angle-of-attack α for an airfoil actuated at frequency $\Omega = 30$ and amplitude $\varepsilon = 0.1$. The excitation clearly suppresses the instability and the oscillations of both h and α decrease over time. Panels (c) and (d) present the time-derivatives of heave $\dot{h}$ and angle-of-attack $\dot{\alpha}$, for the unexcited and excited configurations, respectively. While the effect of rapid oscillations is not directly visible in h or α, the time-derivatives clearly present the higher frequency associated with the forced rapid excitation.

In order to validate the transition curves obtained by the harmonic balance analysis presented in Section 3, large numbers of calculations (similar to the results presented in Fig. 3) were performed for various values of ε and Ω. In order to quantify stability or instability of a specific case, we defined R as the ratio between the amplitude of h or α after 10 oscillation periods and the initial amplitude at $t = 0$. Thus, $R > 1$ represents instability, $R = 1$ is a point on the transition curve and $R < 1$ represents stable configurations. (For example, in the configuration presented in Fig. 3b the amplitudes' ratio equals to $R = 0.04$ and hence flutter is suppressed.) Contour plots of R (based on h) as function of Ω and ε are presented in Fig. 4a. Calculation of R based on α yields nearly identical results and is therefore omitted. The airfoil properties and flight conditions used in the calculations were again set by (7a). The value of R is defined by gray-scale, where the blue line mark numerical calculations yielding $0.95 < R < 1.05$. The red lines mark the analytic transition curves obtained from harmonic balance presented in Section 3. Good agreement between the numerical and analytic transition curves is presented, supporting and validating the analytic results. In addition, in Fig. 4b we present the effect of a predefined values of excitation frequency Ω and amplitude ε on the minimal flight speed yielding flutter instability V_f. A contour plot of minimal flutter speed is presented in terms of $V_f(\varepsilon, \Omega)/V_f(0, 0)$, (where $V_f(0, 0)$ is the flutter speed of the airfoil in the absence of any excitation). The plot was obtained by calculation of stability for each pair of Ω and ε for various flight speeds, and interpolating the minimal unstable flight speed. A significant increase in flutter speed of up to $3V_f(0, 0)$ is presented.

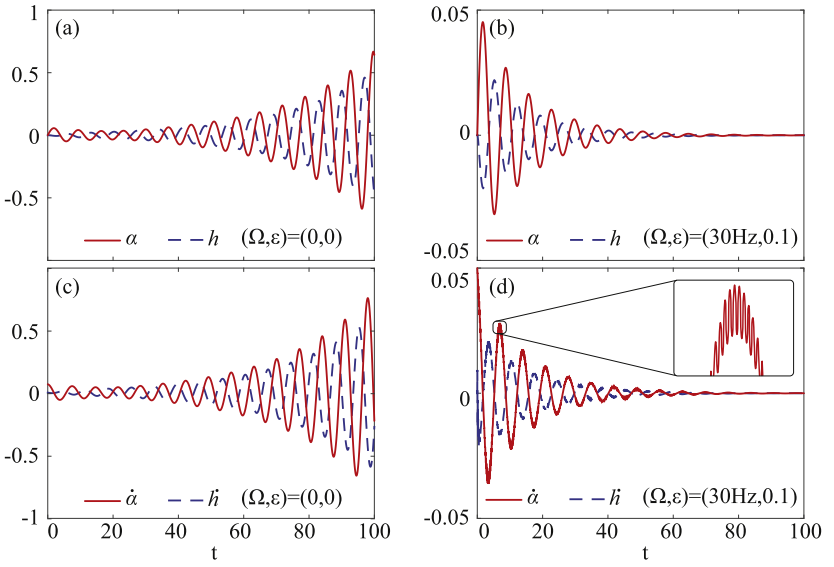

Fig. 3. Numerical solution of (5) with the excitation set to $\Omega = 30$ [Hz] and $\varepsilon = 0.1$. Panels (a) and (b) present α and h. Panels (c) and (d) present $\dot{\alpha}$ and $\dot{h}$. Panels (a) and (c) present the system response for unstable flight conditions without actuation. Panels (b) and (d) present the system response at the same flight conditions with the excitation applied, clearly achieving flutter suppression.

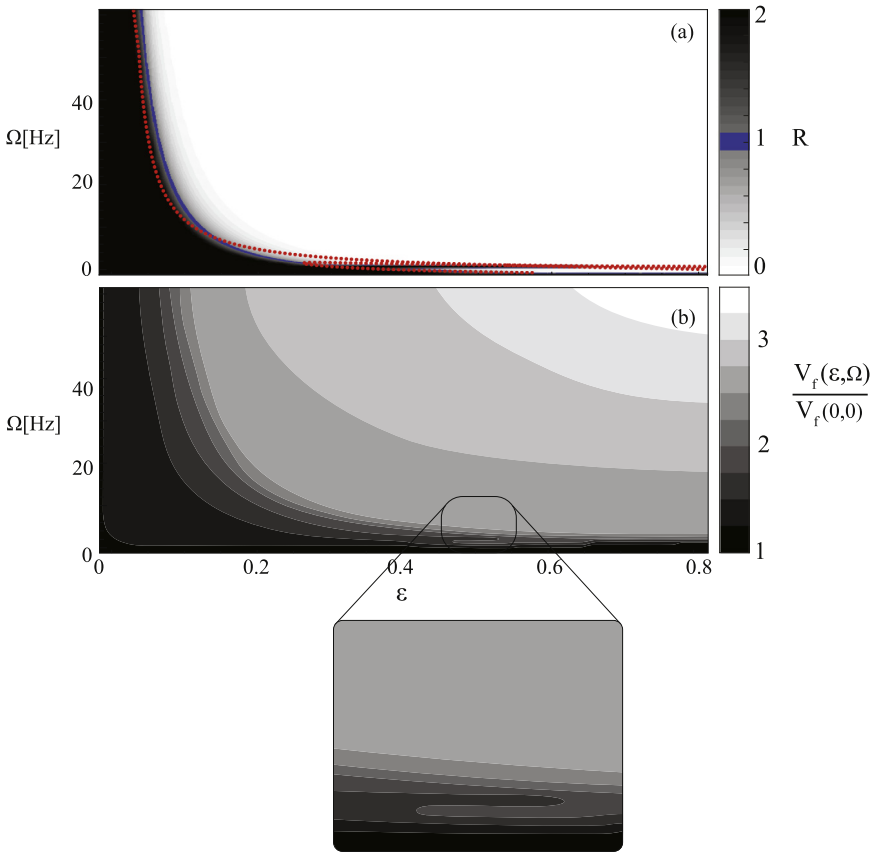

Fig. 4. Maps of the parameter R, representing stability of the configuration ($R > 1$ represents instability, $R < 1$ represents stable configurations). Panels (a) presents stability regions as obtained from the numerical calculation in comparison to the analytic transition curve for two sets of parameters. In panel (a) the distance between the elastic axis and the center-of-mass is 0 ($x_\alpha = 0$). Panel (b) presents the ratio between the minimal flutter speed with excitation at prescribed values of (Ω, ε) and the minimal flutter speed of the unexcited system. Configuration parameters are defined by (7a).. (For interpretation of the references to color in this figure legend, the reader is referred to the web version of this article.)

5. Three-dimensional effects - strip theory approximation

In realistic wing structures it is more practical to implement a mechanism creating forced oscillations only on a specific segment of the wing. In this section we examine the effect of the location of such partial actuation along the wing-span on the amplitude and frequency needed to obtain stabilization. The quasi-3D elastic model used in this section includes an additional degree-of-freedom: a bending angle θ defined in Fig. 5c, along with the previously used heave h and rotation α degrees-of-freedom. The aerodynamic model applies the strip-theory-approximation (Yates, 1958), under which the wing-span is divided into n elements and the known results from the 2D case are employed to calculate the lift and moment for each wing segment.

In order to expand the configuration into a quasi-3D model we used a standard beam element formulation (Bathe and Wilson, 1976, chapter 1), under the assumptions of small deformation, negligible in-plane-bending and axial deformation. In the current calculation the wing is divided into $n = 30$ equal elements of length $l_e = L/n$ (where $L = 10[m]$ is the length of the wing-span). The number of elements was chosen based on convergence analysis, presented in panel 5g. Each element defines 6 degrees-of-freedom,

$$\boldsymbol{q}_i = \begin{Bmatrix} h_i \\ \theta_i \\ \alpha_i \\ h_{i+1} \\ \theta_{i+1} \\ \alpha_{i+1} \end{Bmatrix}, \tag{8}$$

where i and $i+1$ denote both edges of the element. Applying Lagrange's equations (similarly to Section 2) the relevant equations of motion for element i can be written in the form

$$[\boldsymbol{M}]_i\ddot{q}_i + [\boldsymbol{C}]_i\dot{q}_i + [\boldsymbol{K}]_i q_i = [\boldsymbol{Q}_{AD}]_i, \tag{9}$$

(where the matrices $[\boldsymbol{M}]_i$, $[\boldsymbol{C}]_i$, $[\boldsymbol{K}]_i$ and $[\boldsymbol{Q}_{AD}]_i$ are defined in Appendix B, as well as additional details and coefficients used the calculation).

Since each element is coupled to two adjacent elements, a system of $3n$ equations governs the dynamics of the wing. These equations are supplemented by boundary conditions at the clamped root of the airfoil ($[h_0(t), \theta_0(t), \alpha_0(t)] = [0, 0, 0]$), and zero forces and moments at the free-end. Actuation of a segment is obtained by setting r_α to oscillate according to (7a). For simplicity, the wingspan is divided into three equal segments: (1) root segment, (2) middle segment, (3) tip segment. This division allows to compare the efficiency of an oscillation mechanism applied in four different configurations, (1)–(3) as well a full wing actuation (4).

The equations were solved numerically for a range of values of ε and Ω (similarly to calculations in Section 4). Contour plots of the R (calculated based on h) as function of ε and Ω are presented in Fig. 5. Numerically calculated transition lines $R \approx 1$ are marked by blue, light gray marks $R > 1$ (stable conditions), and dark gray marks $R < 1$ (unstable conditions). Panels (a–d) present actuation of the root segment (a), middle segment (b), tip segment (c) and combined actuation of all three segments (d). (See panel (e) for location of the three equal root, middle and tip segments). Panel (f) presents a comparison between the numerical lower transition curves obtained in panels (a–d) and the transition curve obtained in the 2D model.

Actuation of the root segment (panel a) is shown to yield a single transition line (similarly to the 2D results) with a significant increase of the area of unstable conditions compared to the 2D results. Actuation of the middle segment (panel b) reduces the lower unstable region compared with the root actuation case. However, in this case a second transition line emerges, corresponding to a second unstable region bounding the stable region. For actuation of the tip, the lower unstable region decreases further, while the area of upper unstable region increases. From panels (a–c), it is clear that actuation of the tip is significantly more effective. Panel (d) presents full actuation of all segments, yielding minor improvement over actuation of the tip segment only. From panel (f), the quasi-3D model with full actuation is shown to estimate lower stabilization frequencies (compared with the 2D model) for small amplitudes, and higher frequencies in higher amplitudes. Nonetheless, the 2D model and quasi-3D with full actuation model present similar transition lines.

6. Concluding remarks

This work examined rapid vibrations of radius of gyration as a mechanism to suppress flutter instability. Applying harmonic balance analysis on a 2D aeroelastic airfoil, we computed the transition curves between stable and unstable regions by the relevant Hill's determinants. The results were verified by numerical calculations, and extended to include quasi-3D structural effects. The analytic calculations are available as MATHEMATICA® code attached as supplementary material.

The presented numerical computations were made for characteristic aeroelastic values, indicating that such rapid oscillations may be implemented in realistic configurations as a stabilization mechanism. In addition, stabilization by rapid oscillations may be applied by the airfoil's standard control mechanisms. This is specifically relevant to shape-morphing airfoils, which are inherently flexible and able to dynamically change their properties (see Thill et al., 2008; Barbarino et al., 2011 and references therein). Nonetheless, it is clear that additional considerations are needed to be taken into account in

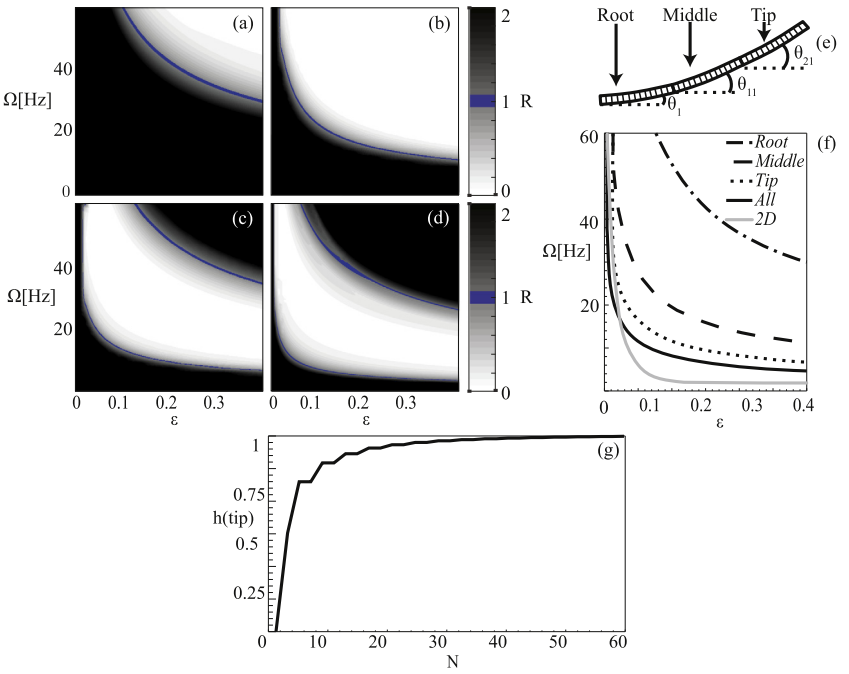

Fig. 5. Numerical calculations of a quasi-3D strip-theory-approximation model, using the same parameters from the 2D model (defined at (7)). Panels (a–d) present R ($R > 1$ in stable conditions, $R < 1$ in unstable conditions) for actuation of the root segment (a), middle segment (b), tip segment (c) and combined actuation of all three segments (d). Panel (e) presents illustration of the three segments used in the strip-theory-approximation. Panel (f) presents comparison between the numerical transition curves obtained in panels (a–d) and the transition curve obtained in the 2D model. Panel (g) presents numerical convergence graph comparing $h(tip)$ heave at the wing tip vs. n the number of elements used in the computation. The heave is scaled according to its value at $N \to \infty$.

order to apply this mechanism in a specific configuration. The main issues to consider are the wing's inner volume assigned to this mechanism, the feasibility of such actuators needed to generate appropriate oscillations and investigating effects of structural damping.

Unlike the standard Kapitza problem, the proposed oscillatory stabilization mechanism modifies the external aerodynamic excitation on the structure, which are modeled via a potential flow approximation. While potential flow models are commonly and successfully used to describe such oscillatory aeroelastic dynamics, the effect of inaccuracies of the model on the stability dynamics were not examined here, and would require further research. Finally, while this paper only studies the effects of excitation in the gyration radius, oscillations of other parameters were examined by the authors. Similar stabilization behavior was obtained by both radius of gyration and center of mass excitation. While rapid oscillation of any other of the airfoil parameters will yield governing differential equations with oscillating coefficients, no stabilization was found for any other actuation parameters except the center-of-mass and gyration-radius.

Appendix A. Theodorsen's theorem

For completeness, the standard Theodorsen calculation used in Section 3 is presented, where

$$L = \pi\rho\left(\ddot{h} + V\dot{\alpha} + ba\ddot{\alpha}\right) + 2\pi\rho VbC(K)\left[\dot{h} + V\alpha + b\left(\frac{1}{2} - a\right)\dot{\alpha}\right] \tag{A.1}$$

$$M = \pi\rho b^2\left[ba\ddot{h} - Vb\left(\frac{1}{2} - a\right)\dot{\alpha} - b^2\left(\frac{1}{2} + a^2\right)\ddot{\alpha}\right] + 2\pi\rho Vb^2\left(\frac{1}{2} + a\right)C(k)\left[\dot{h} + V\alpha + b\left(\frac{1}{2} - a\right)\dot{\alpha}\right] \tag{A.2}$$

In order to simplify the equations we used the definitions used in Bisplinghoff (Bisplinghoff et al., 1957):

$$L_h = C_{L_\alpha}\left(-\frac{k^2}{2} - kG\right) \tag{A.3}$$

$$M_h = C_{L_\alpha}\left[-\frac{k^2 a}{2} - k\left(\frac{1}{2}-a\right)G\right] \tag{A.4}$$

$$L_{\dot{h}} = C_{L_\alpha} F \tag{A.5}$$

$$M_{\dot{h}} = C_{L_\alpha}\left(a+\frac{1}{2}\right)F \tag{A.6}$$

$$L_\alpha = C_{L_\alpha}\left[\frac{k^2 a}{2} + F - Gk\left(\frac{1}{2}-a\right)\right] \tag{A.7}$$

$$M_\alpha = C_{L_\alpha}\left[\frac{k^2}{2}\left(\frac{1}{8}+a^2\right) + F\left(a+\frac{1}{2}\right) + kG\left(a^2-\frac{1}{4}\right)\right] \tag{A.8}$$

$$L_{\dot{\alpha}} = C_{L_\alpha}\left[\frac{1}{2} + F\left(\frac{1}{2}-a\right)\right] \tag{A.9}$$

$$M_{\dot{\alpha}} = C_{L_\alpha}\left[-\frac{1}{2}\left(a-\frac{1}{2}\right) + F\left(a^2-\frac{1}{4}\right) + \frac{G}{k}\left(a+\frac{1}{2}\right)\right] \tag{A.10}$$

$$C(k) = \frac{K_1(ik)}{K_0(ik)+K_1(ik)} \tag{A.11}$$

$$F = Real\{C(k)\}, \; G = Imag\{C(k)\} \tag{A.12}$$

$K_i(ik)$- Is the Bessel function with order i.

Appendix B. Coefficients of the strip theory approximation

For actuated elements (general case of actuation in both x_α and r_α is presented), the matrices in (9) are defined by

$$[\mathbf{Q}_{AD}]_i = l_e \begin{bmatrix} -bL_{\dot{\alpha}} - L_{\dot{h}} & 0 & -eL_{\dot{h}} & -bL_{\dot{\alpha}} - L_{\dot{h}} & 0 & -eL_{\dot{h}} \\ 0 & 0 & 0 & 0 & 0 & 0 \\ b^2 M_{\dot{\alpha}} + bM_{\dot{h}} & 0 & beM_{\dot{h}} & b^2 M_{\dot{\alpha}} + bM_{\dot{h}} & 0 & beM_{\dot{h}} \end{bmatrix} \dot{q}_i + \begin{bmatrix} -bL_\alpha - L_h & 0 & -eL_h & -bL_\alpha - L_h & 0 & -eL_h \\ 0 & 0 & 0 & 0 & 0 & 0 \\ b^2 M_\alpha + bM_h & 0 & beM_h & b^2 M_\alpha + bM_h & 0 & beM_h \end{bmatrix} q_i \tag{B.1}$$

$$[\boldsymbol{M}]_i = \frac{1}{2}\begin{bmatrix} 1 & \frac{l_e}{2} & x_\alpha & 0 & 0 & 0 \\ \frac{l_e}{2} & \frac{I_z}{m_e} + \frac{{l_e}^2}{2} & \frac{l_e}{2}x_\alpha & 0 & 0 & 0 \\ x_\alpha & \frac{l_e}{2}x_\alpha & r_\alpha^2 & 0 & 0 & 0 \\ 0 & 0 & 0 & 1 & -\frac{l_e}{2} & x_\alpha \\ 0 & 0 & 0 & -\frac{l_e}{2} & \frac{I_z}{m_e} + \frac{{l_e}^2}{2} & -\frac{l_e}{2}x_\alpha \\ 0 & 0 & 0 & x_\alpha & -\frac{l_e}{2}x_\alpha & r_\alpha^2 \end{bmatrix} \tag{B.2}$$

$$[\boldsymbol{C}]_i = \frac{1}{2}\begin{bmatrix} 0 & 0 & \dot{x_\alpha} & 0 & 0 & 0 \\ 0 & 0 & \frac{l_e}{2}\dot{x_\alpha} & 0 & 0 & 0 \\ \dot{x_\alpha} & \frac{l_e}{2}\dot{x_\alpha} & \dot{r}_\alpha^2 & 0 & 0 & 0 \\ 0 & 0 & 0 & 0 & 0 & \dot{x_\alpha} \\ 0 & 0 & 0 & 0 & 0 & -\frac{l_e}{2}\dot{x_\alpha} \\ 0 & 0 & 0 & \dot{x_\alpha} & -\frac{l_e}{2}\dot{x_\alpha} & \dot{r}_\alpha^2 \end{bmatrix} \tag{B.3}$$

and

$$[\boldsymbol{K}]_i = \begin{bmatrix} \omega_h^2 & \frac{l_e}{2}\omega_h^2 & 0 & -\omega_h^2 & \frac{l_e}{2} & 0 \\ \frac{l_e}{2}\omega_h^2 & \frac{l_e^2}{3}\omega_h^2 & 0 & -\frac{l_e}{2}\omega_h^2 & \frac{l_e^2}{6}\omega_h^2 & 0 \\ 0 & 0 & \omega_\alpha^2 r_\alpha^2 & 0 & 0 & -\omega_\alpha^2 r_\alpha^2 \\ -\omega_h^2 & -\frac{l_e}{2}\omega_h^2 & 0 & \omega_h^2 & -\frac{l_e}{2} & 0 \\ \frac{l_e}{2}\omega_h^2 & \frac{l_e^2}{6}\omega_h^2 & 0 & -\frac{l_e}{2}\omega_h^2 & \frac{l_e^2}{3}\omega_h^2 & 0 \\ 0 & 0 & -\omega_\alpha^2 r_\alpha^2 & 0 & 0 & \omega_\alpha^2 r_\alpha^2 \end{bmatrix}, \tag{B.4}$$

where

$rho = 1.125\ [\mathrm{Kg/m^3}]$		is air density,
$m = \pi(\mu\rho)b^2L$		is the wing mass (excluding the mechanism),
$m_a = 0.1m$		is the mechanism mass,
$m_e = m/n$		is the segment mass,
$l_e = L/n, L = 10\ [\mathrm{m}]$		is the segment length,
$e = 0.5 - a$		is the distance between the elastic axis and aerodynamic center,
$I_z = \frac{m_e}{12}(l_e^2 + t^2)$		is the max chamber thickness ($t \approx 0.1(2b)$).

All other relevant values are defined in (7a). In the case where an element is not actuated x_α and r_α^2 are both constant and therefore $\dot{x_\alpha} = \dot{r}_\alpha = 0$.

References

Barbarino, S., Bilgen, O., Ajaj, R.M., Friswell, M.I., Inman, D.J., 2011. A review of morphing aircraft. J. Intell. Mater. Syst. Struct. 22 (9), 823–877.

Bathe, K.-J., Wilson, E.L., 1976. Numerical Methods in Finite Element Analysis. Prentice-Hall.

Bisplinghoff, R.L., Ashley, H., Halfman, R.L., 1957. Aeroelasticity. Addisin-Wesley.

Borri, C., Costa, C., Zahlten, W., 2002. Non-stationary flow forces for the numerical simulation of aeroelastic instability of bridge decks. Comput. Struct. 80 (12), 1071–1079.

Caracoglia, L., Jones, N., 2003. Time domain vs. frequency domain characterization of aeroelastic forces for bridge decksections. J. Wind Eng. Ind. Aerodyn. 91 (3), 371–402.

Fabien, B., 2008. Analytical System Dynamics: Modeling and Simulation. Springer Science & Business Media.

Friedmann, P., Guillot, D., Presente, E., 1997. Adaptive control of aeroelastic instabilities in transonic flow and its scaling. J. Guid. Control Dyn. 20 (6), 1190–1199.

Garrick, I., Reed III, W.H., 1981. Historical development of aircraft flutter. J. Aircr. 18 (11), 897–912.

Gu, M., Chang, C., Wu, W., Xiang, H., 1998. Increase of critical flutter wind speed of long-span bridges using tuned mass dampers. J. Wind Eng. Ind. Aerodyn. 73 (2), 111–123.

Hollowell, S.J., Dugundji, J., 1984. Aeroelastic flutter and divergence of stiffness coupled, graphite/epoxy cantilevered plates. J. Aircr. (ISSN 0021-8669) 21, 69–76.

Hsu, C., 1963. On the parametric excitation of a dynamic system having multiple degrees of freedom. J. Appl. Mech. 30 (3), 367–372.

Hübner, B., Walhorn, E., Dinkler, D., 2004. A monolithic approach to fluid–structure interaction using space–time finite elements. Comput. Methods Appl. Mech. Engrg. 193 (23), 2087–2104.

Kameyama, M., Fukunaga, H., 2007. Optimum design of composite plate wings for aeroelastic characteristics using lamination parameters. Comput. Struct. 85 (3), 213–224.

Kapitza, P.L., 1951. A pendulum with oscillating suspension. Uspekhi Fizicheskikh Nauk 44, 7–20.

Karpel, M., 1982. Design for active flutter suppression and gust alleviation using state-space aeroelastic modeling. J. Aircr. 19 (3), 221–227.

Kawai, H., 1998. Effect of corner modifications on aeroelastic instabilities of tall buildings. J. Wind Eng. Ind. Aerodyn. 74, 719–729.

Kuchment, P.A., 2012. Floquet Theory for Partial Differential Equations, Vol. 60. Birkhäuser.

Kwon, S.-D., Park, K.-S., 2004. Suppression of bridge flutter using tuned mass dampers based on robust performance design. J. Wind Eng. Ind. Aerodyn. 92 (11), 919–934.

Lhachemi, H., Chu, Y., Saussié, D., Zhu, G., 2017. Flutter suppression for underactuated aeroelastic wing section: Nonlinear gain-scheduling approach. J. Guid. Control Dyn..

Li, C., 2000. Performance of multiple tuned mass dampers for attenuating undesirable oscillations of structures under the ground acceleration. Earthq. Eng. Struct. Dyn. 29 (9), 1405–1421.
Li, D., Guo, S., Xiang, J., 2012. Study of the conditions that cause chaotic motion in a two-dimensional airfoil with structural nonlinearities in subsonic flow. J. Fluids Struct. 33, 109–126.
Livne, E., 2017. Aircraft active flutter suppression: State of the art and technology maturation needs. J. Aircr. 1–41.
Magnus, W., 1955. Infinite determinants associated with Hill's equatio. Pacific J. Math. 5 (6), 941–951.
Magnus, W., Winkler, S., 2013. Hill's equation. Courier Corporation.
Mickens, R.E., 2010. Truly Nonlinear Oscillations: Harmonic Balance, Parameter Expansions, Iteration, and Averaging Methods. World Scientific.
Ostenfeld-Rosenthal, P., Madsen, H., Larsen, A., 1992. Probabilistic flutter criteria for long span bridges. J. Wind Eng. Ind. Aerodyn. 42 (1), 1265–1276.
Reich, G.W., Raveh, D.E., Zink, P., 2004. Application of active-aeroelastic-wing technology to a joined-wing sensorcraft. J. Aircr. 41 (3), 594–602.
Scanlan, R., 1978. The action of flexible bridges under wind, I: Flutter theory. J. Sound Vib. 60 (2), 187–199.
Thill, C., Etches, J., Bond, I., Potter, K., Weaver, P., 2008. Morphing skins. Aeronaut. J. 112 (1129), 117–139.
Weisshaar, T.A., 1980. Divergence of forward swept composite wings. J. Aircr. 17 (6), 442–448.
Xiang, J., Yan, Y., Li, D., 2014. Recent advance in nonlinear aeroelastic analysis and control of the aircraft. Chin. J. Aeronaut. 27 (1), 12–22.
Yang, Z., Zhao, L., 1988. Analysis of limit cycle flutter of an airfoil in incompressible flow. J. Sound Vib. 123 (1), 1–13.
Yates, Jr., E.C., 1958. Calculation of Flutter Characteristics for Finite-Span Swept or Unswept Wings at Subsonic and Supersonic Speeds by a Modified Strip Analysis. NACA RM L57L10.
Zounes, R.S., Rand, R.H., 1998. Transition curves for the quasi-periodic Mathieu equation. SIAM J. Appl. Math. 58 (4), 1094–1115.